

Trigonal warping and Berry's phase $N\pi$ in ABC-stacked multilayer graphene

Mikito Koshino¹ and Edward McCann²

¹*Department of Physics, Tokyo Institute of Technology,
2-12-1 Ookayama, Meguro-ku, Tokyo 152-8551, Japan*

²*Department of Physics, Lancaster University, Lancaster, LA1 4YB, UK*

The electronic band structure of ABC-stacked multilayer graphene is studied within an effective mass approximation. The electron and hole bands touching at zero energy support chiral quasiparticles characterized by Berry's phase $N\pi$ for N -layers, generalizing the low-energy band structure of monolayer and bilayer graphene. We investigate the trigonal-warping deformation of the energy bands and show that the Lifshitz transition, in which the Fermi circle breaks up into separate parts at low energy, reflects Berry's phase $N\pi$. It is particularly prominent in trilayers, $N = 3$, with the Fermi circle breaking into three parts at a relatively large energy that is related to next-nearest-layer coupling. For $N = 3$, we study the effects of electrostatic potentials which vary in the stacking direction, and find that a perpendicular electric field, as well as opening an energy gap, strongly enhances the trigonal-warping effect. In magnetic fields, the $N = 3$ Lifshitz transition is manifested as a coalescence of Landau levels into triply-degenerate levels.

PACS numbers: 71.20.-b, 81.05.Uw, 73.63.-b, 73.43.Cd.

I. INTRODUCTION

Soon after the fabrication of individual graphene flakes a few years ago [1], it was realized that low-energy quasiparticles in graphene are chiral, with a linear dispersion and degree of chirality characterized by Berry's phase π in monolayer graphene [2, 3] and quadratic dispersion related to Berry's phase 2π in bilayers [4, 5]. In addition to their degree of chirality, bilayers are distinguished from monolayers by the possibility of using doping or external gates to induce interlayer asymmetry that opens a tunable gap between the conduction and valence bands [5, 6, 7, 8, 9, 10, 11], as observed in transport [12, 13] and spectroscopic measurements [14, 15, 16, 17, 18, 19].

Recently, there has been experimental interest in the transport properties of trilayer graphene [20, 21, 22]. It is expected that two different types of stacking order, ABA and ABC (illustrated in Fig. 1), will be realized in nature and that electronic properties will depend strongly on the stacking type. For ABA-stacked trilayer graphene, the low-energy electronic band structure consists of separate monolayer-like and bilayer-like bands [6, 7, 10, 23, 24, 25, 26, 27] that become hybridized in the presence of interlayer asymmetry [7, 26]. By contrast, the low-energy bands of ABC-stacked trilayers [7, 10, 23, 28] do not resemble those of monolayers or bilayers, but appear to be a cubic generalization of them. Thus, there is a cubic dispersion relation and chirality related to Berry's phase 3π [7, 29, 30], and, as in bilayers, the application of interlayer asymmetry is predicted to open an energy gap in the spectrum [7, 10].

In this paper, we show that the low-energy band structure of ABC-stacked multilayer graphene is not just a straightforward generalization of that of monolayers and bilayers. We focus on a particular aspect of the band structure, trigonal warping, which plays a crucial role in the low-energy band structure. Trigonal warping is a deformation of the Fermi circle around a degeneracy point

[31], at each of two inequivalent corners of the hexagonal Brillouin zone that are known as K points [32] [Fig. 1(b)]. In bilayer graphene, trigonal warping is enhanced by the interlayer coupling and leads to a Lifshitz transition [33] when the Fermi line about each K point is broken into several pockets [5, 24, 29, 34, 35, 36, 37, 38]. Here, we develop an effective Hamiltonian for ABC-stacked trilayer graphene, to show that trigonal warping in it is both qualitatively and quantitatively different from that in bilayers. The main contribution to trigonal warping arises from a different type of interlayer coupling that is missing in bilayers and we predict that it leads to a Lifshitz transition at a much larger energy $\sim 10\text{meV}$, which is 10 times as large as in a bilayer. Moreover, on undergoing the Lifshitz transition, the Fermi surface breaks into a different number of pockets reflecting Berry's phase 3π in contrast to 2π in bilayers. Here, we also generalize our approach to describe trigonal warping in general ABC-stacked N -layer graphene, to show that Berry's phase $N\pi$ manifests itself in different characteristics of the Lifshitz transition.

In the next Section, we describe the effective mass model of ABC-stacked trilayer graphene and the resulting band structure. Then, in Section III, we derive an effective low-energy Hamiltonian and we use it to compare the behavior of low-energy chiral quasiparticles in trilayers with those in monolayer and bilayer graphene. In Section IV, we provide an approximate analytical description of the Lifshitz transition in the absence and in the presence of interlayer asymmetry that opens a gap in the spectrum. Section V describes the manifestation of the Lifshitz transition in the degeneracy of Landau levels in the presence of a finite magnetic field. In Section VI, we generalize our approach to ABC-stacked N -layer graphene. Throughout, we compare the approximate description of the effective low-energy Hamiltonian with numerical diagonalization of the full effective mass model.

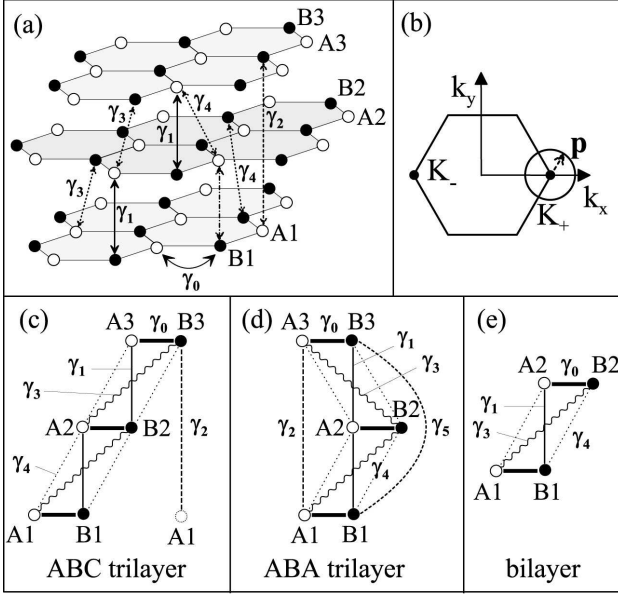


FIG. 1: (a) Schematic of the ABC-stacked trilayer lattice containing six sites in the unit cell, A (white circles) and B (black circles) on each layer, showing the Slonczewski-Weiss-McClure parameterization [39] of relevant couplings γ_0 to γ_4 . (b) Schematic of the hexagonal Brillouin zone with two inequivalent valleys K_{\pm} showing the momentum \mathbf{p} measured from the center of valley K_+ . Schematic of the unit cell of (c) ABC-stacked trilayer graphene, (d) ABA-stacked trilayer graphene, and (e) bilayer graphene. In (c), γ_2 describes a vertical coupling between sites $B3$ and $A1$ in different unit cells.

II. THE EFFECTIVE MASS MODEL OF ABC-STACKED TRILAYER GRAPHENE

The lattice of ABC-stacked trilayer graphene consists of three coupled layers, each with carbon atoms arranged on a honeycomb lattice, including pairs of inequivalent sites $\{A1, B1\}$, $\{A2, B2\}$, and $\{A3, B3\}$ in the bottom, center, and top layers, respectively. The layers are arranged as shown in Fig. 1(a,c), such that pairs of sites $B1$ and $A2$, and $B2$ and $A3$, lie directly above or below each other [for comparison, the unit cell of ABA-stacked graphene is shown in Fig. 1(d)]. In order to write down an effective mass Hamiltonian, we adapt the Slonczewski-Weiss-McClure parameterization of tight-binding couplings of bulk graphite [39]. Nearest-neighbor ($Ai-Bi$ for $i = \{1, 2, 3\}$) coupling within each layer is described by parameter γ_0 , γ_1 describes strong nearest-layer coupling between sites ($B1-A2$ and $B2-A3$) that lie directly above or below each other, γ_3 (γ_4) describes weaker nearest-layer coupling between sites $A1-B2$ and $A2-B3$ ($A1-A2$, $B1-B2$, $A2-A3$, and $B2-B3$). With only these couplings, there would be a degeneracy point at each of two inequivalent corners, K_{\pm} , of the hexagonal Brillouin zone [32] but this degeneracy is broken by next-nearest-layer coupling γ_2 , between sites $A1$ and $B3$ that lie on the same vertical line [10, 23, 28]. For typical values of bulk

ABA graphite we quote [39] $\gamma_0 = 3.16\text{eV}$, $\gamma_1 = 0.39\text{eV}$, $\gamma_2 = -0.020\text{eV}$, $\gamma_3 = 0.315\text{eV}$ and $\gamma_4 = 0.044\text{eV}$. Although the atomic structures of ABA and ABC (rhombohedral) graphite are different, we refer to those values in the following numerical calculations, assuming that the corresponding coupling parameters have similar values [40].

In a basis with atomic components ψ_{A1} , ψ_{B1} , ψ_{A2} , ψ_{B2} , ψ_{A3} , ψ_{B3} , the ABC-stacked trilayer Hamiltonian [7, 28, 40, 41] is

$$\hat{H}_{ABC} = \begin{pmatrix} D_1 & V & W \\ V^\dagger & D_2 & V \\ W^\dagger & V^\dagger & D_3 \end{pmatrix}, \quad (1)$$

where the 2×2 blocks are

$$D_i = \begin{pmatrix} U_i & v\pi^\dagger \\ v\pi & U_i \end{pmatrix} \quad (i = 1, 2, 3), \quad (2)$$

$$V = \begin{pmatrix} -v_4\pi^\dagger & v_3\pi \\ \gamma_1 & -v_4\pi^\dagger \end{pmatrix}, \quad W = \begin{pmatrix} 0 & \gamma_2/2 \\ 0 & 0 \end{pmatrix}, \quad (3)$$

where $v = (\sqrt{3}/2)a\gamma_0/\hbar$, $v_3 = (\sqrt{3}/2)a\gamma_3/\hbar$, $v_4 = (\sqrt{3}/2)a\gamma_4/\hbar$, $\pi = \xi p_x + ip_y$, $\pi^\dagger = \xi p_x - ip_y$, and $\xi = \pm 1$ is the valley index. Here $\mathbf{p} = (p_x, p_y) = p(\cos \phi, \sin \phi)$ is the momentum measured with respect to the center of the valley [Fig. 1(b)]. The parameters U_1 , U_2 , and U_3 describe on-site energies of the atoms on the three layers that may be different owing the presence of substrates, doping, or external gates. In the following, we set the average on-site energy to zero $U_1 + U_2 + U_3 = 0$ and write differences between the on-site energies in terms of asymmetry parameters Δ_1 and Δ_2 [26],

$$\begin{aligned} \Delta_1 &= (U_1 - U_3)/2, \\ \Delta_2 &= (U_1 - 2U_2 + U_3)/6. \end{aligned}$$

Parameter Δ_1 describes a possible asymmetry between the energies of the outer layers, whereas Δ_2 takes into account the possibility that the energy of the central layer may differ from the average outer layer energy.

As there are six atoms in the unit cell, ABC-stacked trilayer graphene has six electronic bands at low energy as plotted in Fig. 2. For no interlayer asymmetry $\Delta_1 = \Delta_2 = 0$, and exactly at the K point, $p = 0$, the eigenvalues ϵ of Hamiltonian Eq. (1) are given by $(\epsilon^2 - \gamma_1^2)^2(\epsilon^2 - \gamma_2^2/4) = 0$. Four of the bands are split away from zero energy by interlayer coupling γ_1 ($\epsilon = \pm\gamma_1$ twice). These high-energy bands correspond to dimer states formed primarily from orbitals on the atomic sites $B1$, $A2$, $B2$, and $A3$ that are strongly coupled by γ_1 . The other two bands ($\epsilon = \pm\gamma_2/2$) are split slightly away from zero energy by next-nearest layer coupling $\gamma_2/2$ that connects atomic sites $A1$ and $B3$ [10, 23, 28].

Figure 2 shows the band structure at several Δ_1 's with $\Delta_2 = 0$, using the parameter values quoted above. Δ_1 opens an energy gap between the lower electron and hole bands, because of the energy difference between $A1$ and

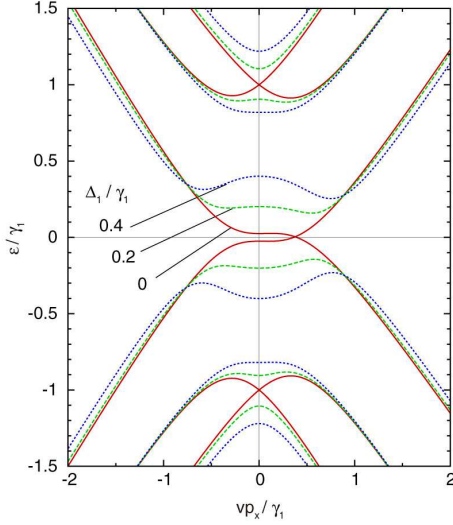


FIG. 2: Band dispersion of ABC-stacked trilayer graphene in the vicinity of K_+ along p_x axis. Parameter values are $\gamma_0 = 3.16\text{eV}$, $\gamma_1 = 0.39\text{eV}$, $\gamma_2 = -0.020\text{eV}$, $\gamma_3 = 0.315\text{eV}$ and $\gamma_4 = 0.044\text{eV}$ [39].

$B3$ sites [7, 10]. Figure 3 shows contour plots of the lower electron band at (a) $\Delta_1/\gamma_1 = 0$ and (b) 0.4 , showing that the band is trigonally warped, and the contour splits into three pockets at low energy. The detailed band structure and its relation to the band parameters will be studied in the following sections.

III. THE LOW-ENERGY EFFECTIVE HAMILTONIAN

To describe the low-energy electronic properties of ABC-stacked trilayer graphene it is useful to derive an effective two-component Hamiltonian that describes hopping between atomic sites $A1$ and $B3$. Such a procedure has been applied to bilayer graphene [5] and to ABC-stacked trilayer graphene [7] for $\gamma_3 = \gamma_2 = \Delta_2 = 0$. We begin with the energy eigenvalue equation $H\Psi = \epsilon\Psi$ of the six-component Hamiltonian, Eq. (1), eliminate the dimer components $\chi = (\psi_{B1}, \psi_{A2}, \psi_{B2}, \psi_{A3})^T$ and, then, simplify the expressions for low-energy components $\theta = (\psi_{A1}, \psi_{B3})^T$ by treating interlayer coupling γ_1 as a large energy scale $|\epsilon|, |vp|, |\gamma_2|, |\gamma_3|, |\gamma_4|, |\Delta_1|, |\Delta_2| \ll \gamma_1$. We denote h_θ as the diagonal block of Hamiltonian of Eq. (1) corresponding to θ , h_χ as the four by four diagonal block corresponding to χ , and u as the off-diagonal 2×4 block coupling θ and χ . The Schrödinger equation for θ can be expanded up to first order in ϵ as $[h_\theta - uh_\chi^{-1}u^\dagger]\theta = \epsilon S\theta$ with $S \equiv 1 + uh_\chi^{-1}u^\dagger$. Then, the effective Hamiltonian for $\tilde{\theta} = S^{1/2}\theta$ becomes $H^{(\text{eff})} \approx S^{-1/2}[h_\theta - uh_\chi^{-1}u^\dagger]S^{-1/2}$.

Thus, we find the following two-component Hamilto-

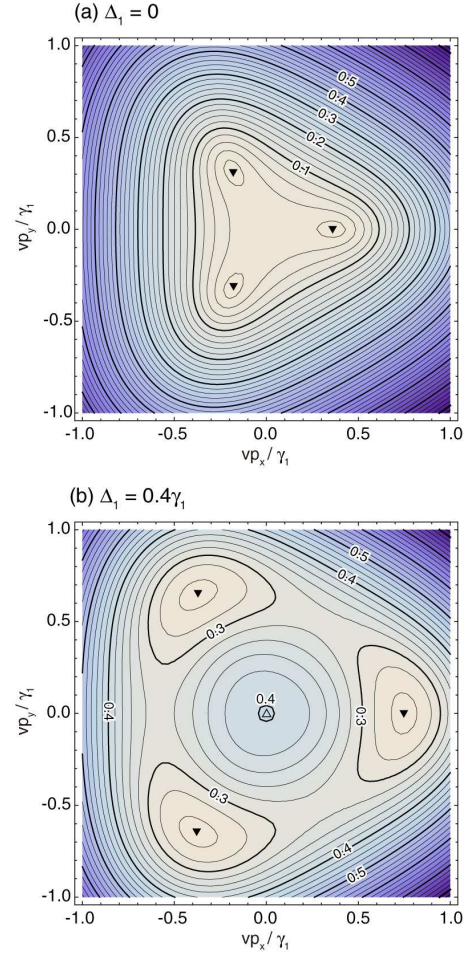


FIG. 3: (a) Equi-energy contour plots of the lowest electron band of ABC trilayer graphene at (a) $\Delta_1 = 0$ and (b) $0.4\gamma_1$. Numbers on the contours indicate energy in units of γ_1 . Filled and empty triangles represent local minima and maxima, respectively, of the energy band.

nian in a basis of the $A1$ - $B3$ sites:

$$\begin{aligned} \hat{H}_{ABC}^{(\text{eff})} &= \hat{H}_3 + \hat{H}_{3w} + \hat{H}_{3c} + \hat{H}_{\Delta 1} + \hat{H}_{\Delta 2}, \\ \hat{H}_3 &= \frac{v^3}{\gamma_1^2} \begin{pmatrix} 0 & (\pi^\dagger)^3 \\ \pi^3 & 0 \end{pmatrix}, \\ \hat{H}_{3w} &= \left(-\frac{2vv_3p^2}{\gamma_1} + \frac{\gamma_2}{2} \right) \begin{pmatrix} 0 & 1 \\ 1 & 0 \end{pmatrix}, \\ \hat{H}_{3c} &= \frac{2vv_4p^2}{\gamma_1^2} \begin{pmatrix} 1 & 0 \\ 0 & 1 \end{pmatrix}, \\ \hat{H}_{\Delta 1} &= \Delta_1 \left(1 - \frac{v^2p^2}{\gamma_1^2} \right) \begin{pmatrix} 1 & 0 \\ 0 & -1 \end{pmatrix}, \\ \hat{H}_{\Delta 2} &= \Delta_2 \left(1 - \frac{3v^2p^2}{\gamma_1^2} \right) \begin{pmatrix} 1 & 0 \\ 0 & 1 \end{pmatrix}. \end{aligned} \quad (4)$$

Here we keep only the leading order for the terms including γ_2 , v_3 and v_4 . Terms \hat{H}_3 and $\hat{H}_{\Delta 1}$ were derived in Ref. [7]. The cubic term \hat{H}_3 describes effective hopping between sites $A1$ and $B3$ via the other sites on the lattice

that are strongly coupled by γ_1 . Taken on its own, it produces a dispersion $\epsilon = \pm v^3 p^3 / \gamma_1^2$. \hat{H}_{3w} arises from the skewed interlayer coupling γ_3 and the next-nearest interlayer coupling γ_2 , and is responsible for trigonal warping as discussed in detail later. \hat{H}_{3c} , coming from another interlayer coupling γ_4 , gives an identical curvature to the electron and hole bands and thus introduces electron-hole asymmetry. Terms $\hat{H}_{\Delta 1}$, $\hat{H}_{\Delta 2}$ arise from the interlayer asymmetries Δ_1 and Δ_2 , respectively. $\hat{H}_{\Delta 1}$ leads to the opening of an energy gap between the conduction and valence bands, while $\hat{H}_{\Delta 2}$ produces electron-hole asymmetry in a similar way as \hat{H}_{3c} . In the two-component basis of $\hat{H}_{ABC}^{(\text{eff})}$, time reversal is described by $\hat{H}^*(\mathbf{p}, \Delta_1, \xi) = \hat{H}(-\mathbf{p}, \Delta_1, -\xi)$ and spatial inversion by $\sigma_x \hat{H}(\mathbf{p}, \Delta_1, \xi) \sigma_x = \hat{H}(-\mathbf{p}, -\Delta_1, -\xi)$. Manes *et al* [29] showed that the Fermi points of ABC-stacked multilayers are stable with respect to the opening of a gap against perturbations that respect combined time reversal and spatial inversion, as well as translation invariance.

The low-energy effective Hamiltonian for ABC-stacked trilayer graphene bears some resemblance to that of bilayer graphene [5]. In the lattice of bilayer graphene, Fig. 1(e), two of the sites ($B1$ and $A2$) are directly above or below each other and are strongly coupled by interlayer coupling γ_1 whereas two sites ($A1$ and $B2$) do not have a counterpart in the other layer. The low-energy Hamiltonian is written in a basis (ψ_{A1}, ψ_{B2}) of these two sites:

$$\begin{aligned} \hat{H}_{AB}^{(\text{eff})} &= \hat{H}_2 + \hat{H}_{2w} + \hat{H}_{\Delta}, \\ \hat{H}_2 &= -\frac{v^2}{\gamma_1} \begin{pmatrix} 0 & (\pi^\dagger)^2 \\ \pi^2 & 0 \end{pmatrix}, \\ \hat{H}_{2w} &= v_3 \begin{pmatrix} 0 & \pi \\ \pi^\dagger & 0 \end{pmatrix}, \\ \hat{H}_{2c} &= \frac{2vv_4 p^2}{\gamma_1^2} \begin{pmatrix} 1 & 0 \\ 0 & 1 \end{pmatrix}, \\ \hat{H}_{\Delta} &= \Delta \left(1 - \frac{2v^2 p^2}{\gamma_1^2} \right) \begin{pmatrix} 1 & 0 \\ 0 & -1 \end{pmatrix}, \end{aligned} \quad (5)$$

where parameter Δ describes interlayer asymmetry between on-site energy Δ of the atoms, $A1$ and $B1$, on the first layer and $-\Delta$ of the atoms, $A2$ and $B2$, on the second layer.

The first term in each Hamiltonian, \hat{H}_2 for bilayers, Eq. (5), and \hat{H}_3 for ABC-stacked trilayers, Eq. (4), are members of a family of Hamiltonians $\hat{H}_J = F(p) \boldsymbol{\sigma} \cdot \mathbf{n}$ where $\mathbf{n} = \mathbf{I}_x \cos(J\xi\phi) + \mathbf{I}_y \sin(J\xi\phi)$ for $\mathbf{p} = p(\cos\phi, \sin\phi)$ [5, 7, 29, 30]. They describe chiral quasiparticles, and the degree of chirality is $J = 1$ in monolayer graphene, $J = 2$ in a bilayer, and, here, $J = 3$ in ABC-stacked trilayer. Quasiparticles described by the Hamiltonians \hat{H}_J acquire a Berry's phase $-i \oint_C d\mathbf{p} \cdot \langle \Psi | \nabla_{\mathbf{p}} | \Psi \rangle = J\xi\pi$, upon an adiabatic propagation along an equi-energetic line C . Thus charge carriers in ABC-stacked trilayer graphene are Berry's phase $3\xi\pi$ quasiparticles, in contrast to Berry's phase $\xi\pi$ particles in monolayers, $2\xi\pi$

in bilayers. As well as the first term in the Hamiltonian Eq. (4) of ABC-trilayers being a generalization of that in bilayers, the influence of interlayer asymmetry $\Delta_1 = (U_1 - U_3)/2$ as described by $\hat{H}_{\Delta 1}$ is similar to that in bilayers as described by \hat{H}_{Δ} , Eq. (5).

IV. TRIGONAL WARPING AND THE LIFSHITZ TRANSITION

In a similar way to bulk graphite [39], the parameter γ_3 [where $v_3 = (\sqrt{3}/2)a\gamma_3/\hbar$] produces trigonal warping in bilayer graphene [5], where the equi-energetic line around each valley is stretched in three directions. This is due to the interference of the matrix elements connecting $A1$ and $B2$, where an electron hopping from $A1$ to $B2$ acquires a factor $e^{2i\xi\phi}$ in \hat{H}_2 and $e^{-i\xi\phi}$ in \hat{H}_{2w} . We neglect the terms including v_4 which add a term $\propto p^2$ to the energy but don't contribute to trigonal warping. At $\Delta = 0$, the eigenenergy of Eq. (5) is given by

$$\epsilon \approx \pm \sqrt{v_3^2 p^2 - 2\xi \frac{v_3 v^2 p^3}{\gamma_1} \cos 3\phi + \frac{v^4 p^4}{\gamma_1^2}}. \quad (6)$$

The warping has a dramatic effect when \hat{H}_2 and \hat{H}_{2w} have comparable amplitudes, i.e., $v^2 p^2 / \gamma_1 \sim v_3 p$, which is satisfied at $p \sim p_0 = \gamma_1 v_3 / v^2$. It leads to a Lifshitz transition [5, 24, 29, 33, 34, 35, 36, 37, 38], in which the equi-energetic line is broken into four separate pockets. There is one central pocket located around $p = 0$ and, three "leg" pockets centered at momentum of magnitude $p = p_0$ and angle $\phi_0 = 2n\pi/3 + (1 - \xi)\pi/6$. The Fermi pocket separation occurs at energy $\epsilon_L = (v_3/v)^2 \gamma_1/4$, which is estimated to be $\epsilon_L \sim 1\text{meV}$.

In ABC-stacked trilayer graphene, there is a similar, but much greater warping effect. In hopping from $A1$ to $B3$, an electron acquires a factor $e^{3i\xi\phi}$ from \hat{H}_3 and a factor of unity from \hat{H}_{3w} , giving trigonal symmetry in ϕ . At $\Delta_1 = \Delta_2 = 0$, the eigenenergy of Eq. (4) reads,

$$\epsilon \approx \pm \sqrt{f(p)^2 + 2\xi f(p) g(p) \cos 3\phi + g(p)^2}, \quad (7)$$

where $f(p) = v^3 p^3 / \gamma_1^2$ comes from \hat{H}_3 and $g(p) = -2vv_3 p^2 / \gamma_1 + \gamma_2/2$ from \hat{H}_{3w} . Similarly to the bilayer, the warping effect is prominent when $|g(p)| \sim f(p)$, or $p \sim p_0$ with $vp_0/\gamma_1 \equiv [\gamma_2/(2\gamma_1)]^{1/3} - (v_3/v)/3$. This estimate is valid as long as $|v_3/v| \lesssim |\gamma_2/\gamma_1|^{1/3}$, which holds for typical parameter values of bulk graphite [39].

The major difference from the bilayer is the contribution of the parameter $\gamma_2/2$, which appears in the Hamiltonian without an accompanying momentum-dependent factor and, thus, it doesn't vanish at $p = 0$. Such trigonal warping produces a Lifshitz transition at low energy, but, unlike bilayers, it occurs at energy $\epsilon_L \approx |\gamma_2/2|$. Although the value of γ_2 in ABC-trilayer graphene has not been measured experimentally, comparison with similar couplings in bulk graphite [39] suggest that $|\gamma_2| \sim 20\text{meV}$.

This opens up the possibility that the Lifshitz transition in ABC-trilayer graphene could occur at a much higher energy than that in bilayers. At energy lower than $|\gamma_2|/2$, the contour splits into three leg pockets centered at $p \sim p_0$ in a trigonal manner. Unlike bilayer graphene, the central pocket is missing because \hat{H}_{γ_2} does not vanish at $p = 0$.

An effective Hamiltonian in the vicinity of the leg pockets, for $|\epsilon| \ll \epsilon_L$, may be obtained by transforming to momentum $\mathbf{q} = (q_x, q_y)$ measured from their centers,

$$q_x = p_x \cos \phi_0 + p_y \sin \phi_0 - p_0, \quad (8)$$

$$q_y = -p_x \sin \phi_0 + p_y \cos \phi_0, \quad (9)$$

and taking the limit of infinitely large γ_1 :

$$\hat{H}_{ABC}^{\text{leg}} = 3v \left| \frac{\gamma_2}{2\gamma_1} \right|^{2/3} \begin{pmatrix} 0 & \xi \alpha q_x - i q_y \\ \xi \alpha q_x + i q_y & 0 \end{pmatrix}, \quad (10)$$

where $\alpha = 1 + (4v_3/3v)(2\gamma_1/\gamma_2)^{1/3}$. Thus, the pockets are elliptical with dispersion $\epsilon \approx \pm 3|\gamma_2/(2\gamma_1)|^{2/3} v \sqrt{\alpha^2 q_x^2 + q_y^2}$. The different nature of the Lifshitz transition in bilayers and ABC-stacked trilayers is a manifestation of Berry's phase. In trilayer graphene, the geometrical phase integrated around the equi-energy line of each pocket is $\xi\pi$ as in a monolayer, giving $3\xi\pi$ in total. This is different from bilayers, where $3\xi\pi$ arises from three leg pockets and $-\xi\pi$ from the center pocket gives $2\xi\pi$ in total [29, 37].

Interlayer asymmetry Δ_1 opens a gap in the spectrum and produces a Mexican hat feature in the low-energy dispersion. [7] The eigenenergy corresponding to Eq. (4) is given by

$$\epsilon \approx \pm \sqrt{f(p)^2 + 2\xi f(p) g(p) \cos 3\phi + g(p)^2 + h(p)^2}, \quad (11)$$

with an extra term as compared to Eq. (7), $h(p) = \Delta_1(1 - v^2 p^2/\gamma_1^2)$, coming from \hat{H}_{Δ_1} . For no trigonal warping [$g(p) = 0$], it yields $\epsilon^2 = \Delta_1^2(1 - v^2 p^2/\gamma_1^2)^2 + v^6 p^6/\gamma_1^4$. The energy is $\epsilon = \pm \Delta_1$ at zero momentum, but there is a minima located isotropically about the center of the valley at finite momentum $p = p_1 \approx (2/3)^{1/4} \sqrt{|\Delta_1 \gamma_1|}/v$ (for $|\Delta_1| \ll |\gamma_1|$) at which the energy is $\epsilon = \epsilon_1 \approx \pm \Delta_1(1 - (2/3)^{3/2} |\Delta_1/\gamma_1|)$.

In the presence of trigonal warping, there is an interplay between the Mexican hat feature and the Lifshitz transition. In the large gap regime, such that $|g| \ll f, h$, the circular edge of the band bottom is trigonally distorted by the perturbation of $g(p)$, making three pockets on it. The bottom of the pockets moves to momentum $p = p_1 + \delta p_1$ with $v\delta p_1/\gamma_1 \approx (\sqrt{6}/8)[\gamma_2/(2\Delta_1)] - (5/6)(v_3/v)$, and energy $\epsilon = \epsilon_1 - \delta\epsilon_1$ with $\epsilon_1 = (2/3)^{3/4} \sqrt{\Delta_1/\gamma_1} |\gamma_2/2 - \sqrt{8/3}(v_3/v)\Delta_1|$. The area of the pocket in k-space becomes of the order of $p_1 \delta p_1$, and the depth in energy is of order $\delta\epsilon_1$, both of which increase as Δ_1 increases. This significant enlargement of the trigonal pockets, in the presence of finite Δ_1 ,

is illustrated in Figure 3 which is produced by numerical diagonalization of the full Hamiltonian Eq. (1). Note that similar widening of the pockets by the gap term occurs in bilayer graphene as well. This can be understood in an analogous way, by writing $f(p) = v^2 p^2/\gamma_1$, $g(p) = v_3 p$, and $h(p) = \Delta(1 - 2v^2 p^2/\gamma_1^2)$.

V. LANDAU LEVEL SPECTRUM

The energy levels in a magnetic field are given by replacing \mathbf{p} with $\mathbf{p} + e\mathbf{A}$ in the Hamiltonian Eq. (1), where $\mathbf{A}(\mathbf{r})$ is the vector potential corresponding to the magnetic field. Here we consider a uniform magnetic field B applied along $+z$ direction in a Landau gauge $\mathbf{A} = (0, Bx)$. Operators π and π^\dagger are then related to raising and lowering operators a^\dagger and a of the Landau level in a conventional two-dimensional system, such that $[l_B/(\sqrt{2}\hbar)]\pi^\dagger = a^\dagger$ and a for K_+ and K_- , respectively, with $l_B = \sqrt{\hbar/(eB)}$. The operator a acts as $a\varphi_{n,k} = \sqrt{n}\varphi_{n-1,k}$, and $a\varphi_0 = 0$, where $\varphi_{n,k}(x, y) \propto e^{iky} e^{-z^2/2} H_n(z)$ is the wavefunction of the n th Landau level in a conventional two-dimensional system with $z = (x + kl_B^2)/l_B$, and H_n being a Hermite polynomial.

In the simplest model including only γ_0 and γ_1 without trigonal warping, the effective Hamiltonian \hat{H}_3 in Eq. (4) yields the eigenstates for K_+ [7]

$$\begin{aligned} \epsilon_n &= 0, \quad \Psi_{nk} \propto \begin{pmatrix} \varphi_{n,k} \\ 0 \end{pmatrix} \quad (n = 0, 1, 2), \\ \left. \begin{aligned} \epsilon_{sn} &= s \frac{\Delta_B^3}{\gamma_1^2} \sqrt{n(n-1)(n-2)} \\ \Psi_{snk} &\propto \begin{pmatrix} \varphi_{n,k} \\ s\varphi_{n-3,k} \end{pmatrix} \end{aligned} \right\} \quad (n \geq 3), \quad (12) \end{aligned}$$

where $s = \pm 1$ describes the electron and hole levels, respectively, $\Delta_B = \sqrt{2\hbar v^2 e B}$. The eigenstates $n = 0, 1, 2$ have a non-zero amplitude only on the first element ($A1$), and remain at zero energy regardless of the magnetic field strength, while the energy of the other levels behaves as $\propto B^{3/2}$. At the other valley K_- , there is a similar structure except that the first and second elements are interchanged, i.e., the zero-energy Landau levels have amplitudes only on sites $B3$ [7].

Trigonal warping gives a remarkable feature in the structure of Landau levels. In enough small fields, the three leg pockets independently accommodate an equal number of Landau levels so that they are triply degenerate. This is in contrast to bilayer graphene where the central pocket also contributes to the degeneracy [5]. The low-energy effective Hamiltonian, Eq. (10), shows that the Landau level energy follows a similar sequence as that in monolayer graphene, $\epsilon_n = 3|\gamma_2/(2\gamma_1)|^{2/3} \sqrt{\alpha} \Delta_B \text{sgn}(n) \sqrt{n}$ where n is integer. The total number of Landau levels accommodated in each pocket is roughly estimated by the condition $\epsilon_n \sim |\gamma_2|/2$, as $n \sim (\gamma_1/\Delta_B)^2 [\gamma_2/(2\gamma_1)]^{2/3}/(9\alpha)$.

Fig. 4(a) shows the Landau level spectrum at the valley K_+ as a function of $\Delta_B (\propto \sqrt{B})$, numerically calculated for the full parameter model Eq. (1) at $\Delta_1 = \Delta_2 = 0$. Below $\epsilon = \gamma_2/2$, the Landau levels are triply degenerate and move in proportion to \sqrt{B} . The degeneracy of each level is broken at $\epsilon = \gamma_2/2$, and it splits into three separate levels, corresponding to coalescence of the leg pockets at the Lifshitz transition. At even higher energy, it approaches $B^{3/2}$ behavior as described in Eq. (12). The triply degenerate level around zero energy is regarded as the $n = 0$ level in each of three pockets. In actual fact, its degeneracy is split slightly in a large magnetic field, owing to magnetic break down among the semi-classical orbits in the leg pockets, which is caused by the parameter v_4 . When the trigonal warping vanishes, those three levels switch to the degenerate levels with indices $n = 0, 1, 2$ in Eq. (12).

Fig. 4(b) shows the Landau level spectrum at K_+ as a function of asymmetry Δ_1 with fixed magnetic field $\Delta_B = 0.1\gamma_1$ ($B \sim 1\text{T}$). As Δ_1 is changed from negative to positive, three Landau levels [indicated by the single diagonal line that crosses $\epsilon = 0$ at $\Delta_1 = 0$ in Fig. 4(b)] are pumped from the hole side to the electron side. In the approximate model of Eq. (12), this corresponds to the fact that the energy levels $n = 0, 1, 2$ have a wave amplitude only on $A1$, so that it acquires on-site energy $+\Delta_1$ in the first order of perturbation. At the other valley K_- , there is the opposite movement, i.e., the three levels go down from positive to negative energies in increasing Δ_1 .

The energy of the Lifshitz transition appears as a region where the levels are densely populated, and below that energy the levels are triply degenerate [indicated by the shaded region in Fig. 4(b)]. It should be noted that the number of triply-degenerate levels increases for larger Δ_1 , reflecting the enlargement of the trigonal pockets discussed above. In a measurement of Hall conductivity, those triply-degenerate Landau levels would be observed as quantum Hall steps of magnitude $3g_v g_s e^2/h$, where $g_v = g_s = 2$ are the valley and spin degeneracies, respectively.

VI. GENERAL ABC-STACKED MULTILAYER GRAPHENE

The analysis of ABC-stacked trilayer graphene can be extended to multilayers with N layers. We consider each layer to consist of carbon atoms on a honeycomb lattice, and the layers are arranged with ABC stacking. The Hamiltonian is written in a basis $\psi_{A1}, \psi_{B1}, \psi_{A2}, \psi_{B2},$

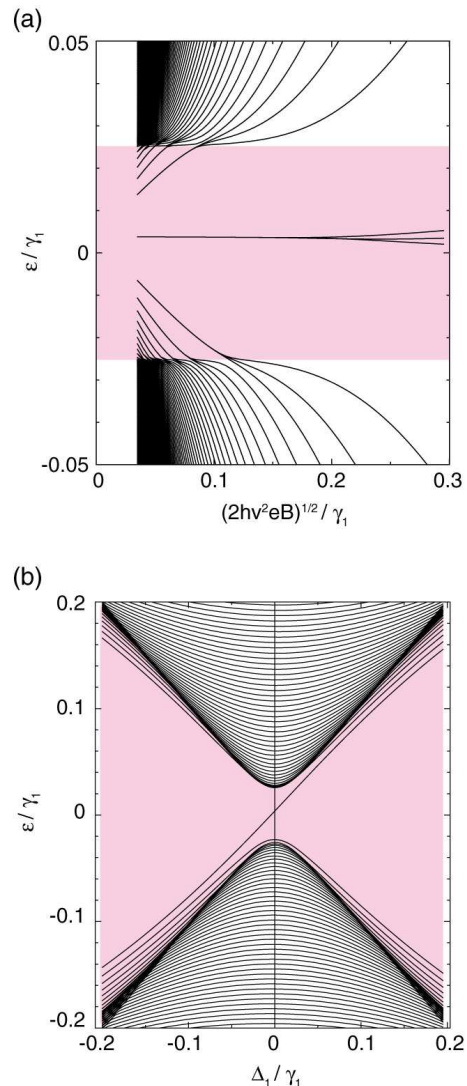


FIG. 4: Landau levels of ABC trilayer graphene, plotted against (a) $B^{1/2}$ at fixed $\Delta_1 = 0$, and (b) Δ_1 at fixed magnetic field $(2\hbar v^2 e B)^{1/2} = 0.1\gamma_1$ ($B \sim 1\text{T}$). The region in which Landau levels are triply degenerate is highlighted by shading.

$\dots, \psi_{AN}, \psi_{BN}$, as [40, 41]

$$\hat{H}_N = \begin{pmatrix} D_1 & V & W & & \\ V^\dagger & D_2 & V & W & \\ W^\dagger & V^\dagger & D_3 & \ddots & \ddots \\ & W^\dagger & \ddots & \ddots & \\ & & & \ddots & \ddots \end{pmatrix}, \quad (13)$$

where the 2×2 blocks D_i, V, W are defined in Eqs. (2,3). Pairs of sites $B(i)$ and $A(i+1)$ ($i = 1, \dots, N-1$) are vertically above or below each other, and are strongly coupled by γ_1 giving dimer states. Thus, all the sites in the lattice, except two, contribute to bands that lie away from zero energy. The remaining two sites, A_1 and B_N , form the lowest-energy electron and hole bands.

Note that these sites lie on the outer layers, so that the lowest bands are missing in an infinite system with periodic boundary conditions applied in the stacking direction. The band structure has trigonal symmetry for any N . This is checked by applying the transformation $\phi \rightarrow \phi + 2\pi/3$ to Eq. (13), where the change in the matrix elements can be canceled by the gauge transformation $\tilde{\psi}_{An} = \alpha_n \psi_{An}$ and $\tilde{\psi}_{Bn} = \alpha_n \psi_{Bn}$, with $\alpha_n = e^{i\xi 2n\pi/3}$.

The effective low-energy Hamiltonian is obtained by treating terms other than γ_1 as perturbations. The effective Hamiltonian in a basis $\{\psi_{A1}, \psi_{BN}\}$ reads

$$\hat{H}_N^{(\text{eff})} = \begin{pmatrix} 0 & X(p) \\ X^\dagger(p) & 0 \end{pmatrix} + \frac{2vv_4p^2}{\gamma_1^2} \begin{pmatrix} 1 & 0 \\ 0 & 1 \end{pmatrix},$$

$$X(p) = \sum_{\{n_1, n_2, n_3\}} \frac{(n_1 + n_2 + n_3)!}{n_1!n_2!n_3!} \frac{1}{(-\gamma_1)^{n_1+n_2+n_3-1}} \times$$

$$(vpe^{i\xi\phi})^{n_1} (v_3pe^{-i\xi\phi})^{n_2} \left(\frac{\gamma_2}{2}\right)^{n_3}, \quad (14)$$

where the summation is taken over positive integers which satisfy $n_1 + 2n_2 + 3n_3 = N$. Here we collected all the higher order terms not including v_4 , but retain just the leading term for v_4 . The trigonal warping structure can be described well in this treatment as shown below, since v_4 only gives the circularly-symmetric band curvature as in ABC trilayer.

The eigenenergies are given by $\varepsilon = 2vv_4p^2/\gamma_1^2 \pm |X(p)|$. If we neglect γ_2 and v_3 , we have $X = (vpe^{i\xi\phi})^N/(-\gamma_1)^{N-1}$ which gives a pair of bands, isotropic in momentum, which touch at the origin [5, 7, 29, 30]. Berry's phase integrated along an energy contour is $N\xi\pi$ at every energy. Perturbation by γ_2 and v_3 produces trigonal warping as observed in the trilayer. Figure 5 shows the lower energy band structure for $\phi = 0$ at several N 's, where the solid lines are calculated using the original Hamiltonian Eq. (13), and the dashed lines use Eq. (14). We can see that the effective Hamiltonian reproduces the original band structure rather well including the positions of the band touching points, except that the magnitude in energy tends to be overestimated around $vp \sim \gamma_1$ where the perturbative approach fails.

The band touching points, or Dirac points, are given by the solution of $X(p) = 0$. They appear in a series of p 's at only three angles $\phi_0 = 2n\pi/3 + (1-\xi)\pi/6$, and around which the Hamiltonian has a chiral structure similar to monolayer graphene. We empirically found that the arrangement of these points obeys the following rules: We have $[(N+1)/3]$ Dirac points at $p \neq 0$ at each of three angles, and each of them has Berry's phase $\xi\pi$. Here $[x]$ represents the greatest integer which does not exceed x . The Dirac point at the center ($p = 0$) only appears when N is not a multiple of 3, and its Berry's phase is $\xi\pi$ and $-\xi\pi$ when $N \equiv 1$ and $-1 \pmod{3}$ respectively. The total Berry's phase summed over all Dirac points is always $N\xi\pi$, the same as the value without trigonal warping. The energy scale for fine structure around the Dirac points becomes smaller as N increases, because the

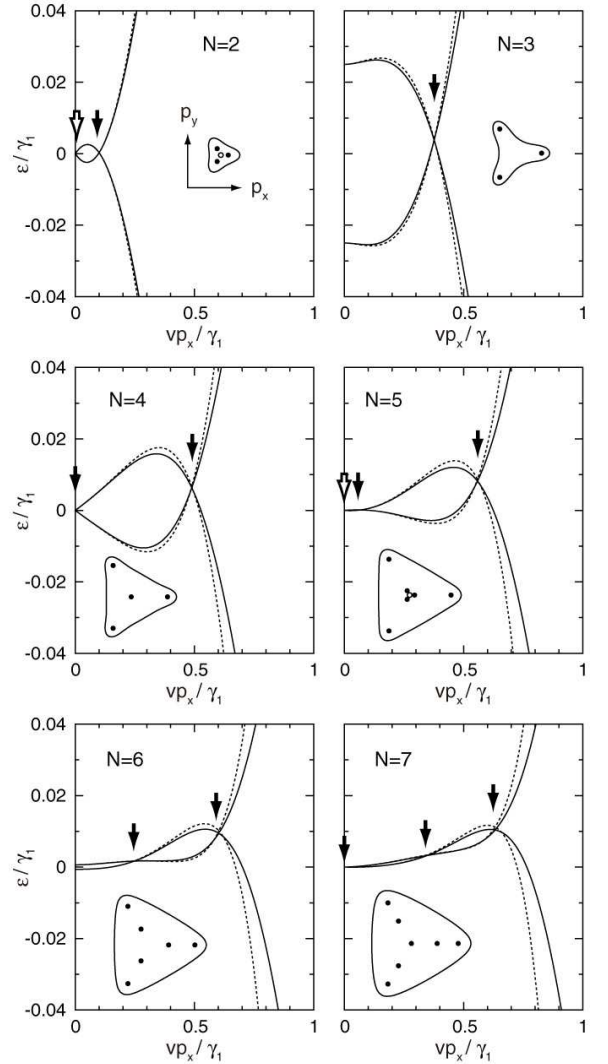


FIG. 5: Low-energy band structure of ABC-stacked multilayer graphene for several different layer numbers N , at $\Delta_1 = \Delta_2 = 0$. Solid and dashed curves are calculated using Eq. (13) and its approximation Eq. (14), respectively. Insets show the equi-energy lines at $\varepsilon = 0.04\gamma_1$. The black and white arrows (circles in insets) represent Dirac points having Berry's phase $\xi\pi$ and $-\xi\pi$, respectively.

matrix elements connecting A_1 and B_N become higher order in p for larger N . We see that $N = 3$ has the most prominent structure, where γ_2 directly connects A_1 and B_N . The parameter v_4 never opens a gap at the Dirac points but gives an energy shift by $2vv_4p^2/\gamma_1^2$ and associated band curvature, leading to misalignment of the Dirac point energies as shown in Fig. 5. The curvature is independent of N because it is due to the second order process from A_1 or B_N to the nearest-neighboring dimer state.

The approach applied to the Landau levels of the trilayer in Sec. V can be extended to the N -layer case. In the simplest model including only γ_0 and γ_1 , the Landau

levels at K_+ read

$$\epsilon_n = 0, \quad \Psi_{nk} \propto \begin{pmatrix} \varphi_{n,k} \\ 0 \end{pmatrix} \quad (n = 0, 1, \dots, N-1), \quad (15)$$

$$\left. \begin{aligned} \epsilon_{sn} &= s \frac{\Delta_B^N}{\gamma_1^{(N-1)}} \sqrt{n(n-1) \cdots (n-N+1)} \\ \Psi_{snk} &\propto \begin{pmatrix} \varphi_{n,k} \\ s\varphi_{n-N,k} \end{pmatrix} \end{aligned} \right\} \quad (n \geq N), \quad (16)$$

with $s = \pm 1$. The first and second elements are again interchanged at the other valley K_- . The zero-energy level is now N -fold degenerate per valley and per spin [7, 29, 30]. In presence of trigonal warping and v_4 , however, this is expected to split in accordance with the discrepancy between the energies of different Dirac points shown in Fig. 5 for $B = 0$, while some levels keep three-fold degeneracy owing to trigonal symmetry as in the trilayer case. It is possible that electronic interactions may create exotic collective modes in such highly-degenerate Landau levels, but we leave the discussion of this for future studies.

VII. CONCLUSIONS

In ABC-stacked multilayer graphene with N layers, two low-energy bands in the vicinity of each valley are

formed from two electronic orbitals that lie on the bottom and top layers of the system. Such bands support chiral quasiparticles corresponding to Berry's phase $N\pi$ [5, 7, 29, 30]. The interplay between different types of interlayer coupling produces trigonal warping, in which the Fermi circle around each valley is stretched in three directions. At very low energy, trigonal warping leads to a Lifshitz transition [33] when the Fermi circle breaks up into separate pockets, in such a way that the total Berry's phase is conserved. We predict that the Lifshitz transition is particularly prominent in trilayers, $N = 3$, with the Fermi circle breaking into three parts at a relatively large energy that is related to next-nearest-layer coupling.

VIII. ACKNOWLEDGMENTS

The authors thank T. Ando, V. I. Fal'ko, and H. Schomerus for discussions. This project has been funded by EPSRC First Grant EP/E063519/1, the Royal Society, and the Daiwa Anglo-Japanese Foundation, and by Grants-in-Aid for Scientific Research from the Ministry of Education, Culture, Sports, Science and Technology, Japan.

-
- [1] K. S. Novoselov, A. K. Geim, S. V. Morozov, D. Jiang, Y. Zhang, S. V. Dubonos, I. V. Grigorieva, A. A. Firsov, *Science* **306**, 666 (2004).
 - [2] K. S. Novoselov, A. K. Geim, S. V. Morozov, D. Jiang, M. I. Katsnelson, I. V. Grigorieva, S. V. Dubonos, and A. A. Firsov, *Nature* **438**, 197 (2005).
 - [3] Y. Zhang, Y.-W. Tan, H. L. Stormer, and P. Kim, *Nature* **438**, 201 (2005).
 - [4] K. S. Novoselov, E. McCann, S. V. Morozov, V. I. Fal'ko, M. I. Katsnelson, U. Zeitler, D. Jiang, F. Schedin, and A. K. Geim, *Nat. Phys.* **2**, 177 (2006).
 - [5] E. McCann and V.I. Fal'ko, *Phys. Rev. Lett.* **96**, 086805 (2006).
 - [6] C. L. Lu, C. P. Chang, Y. C. Huang, R. B. Chen, and M. L. Lin, *Phys. Rev. B* **73**, 144427 (2006).
 - [7] F. Guinea, A. H. Castro Neto, and N. M. R. Peres, *Phys. Rev. B* **73**, 245426 (2006).
 - [8] E. McCann, *Phys. Rev. B* **74**, 161403(R) (2006).
 - [9] H. Min, B. R. Sahu, S. K. Banerjee, and A. H. MacDonald, *Phys. Rev. B* **75**, 155115 (2007).
 - [10] M. Aoki and H. Amawashi, *Solid State Commun.* **142**, 123 (2007).
 - [11] P. Gava, M. Lazzeri, A. M. Saitta and F. Mauri, *Phys. Rev. B* **79**, 165431 (2009).
 - [12] E. V. Castro, K. S. Novoselov, S. V. Morozov, N. M. R. Peres, J. M. B. Lopes dos Santos, Johan Nilsson, F. Guinea, A. K. Geim, and A. H. Castro Neto, *Phys. Rev. Lett.* **99**, 216802 (2007).
 - [13] J. B. Oostinga, H. B. Heersche, X. Liu, A. F. Morpurgo, and L. M. K. Vandersypen, *Nat. Mater.* **7**, 151 (2007).
 - [14] T. Ohta, A. Bostwick, T. Seyller, K. Horn, and E. Rotenberg, *Science* **313** (2006) 951.
 - [15] Z. Q. Li, E. A. Henriksen, Z. Jiang, Z. Hao, M. C. Martin, P. Kim, H. L. Stormer, and D. N. Basov, *Phys. Rev. Lett.* **102**, 037403 (2009).
 - [16] L. M. Zhang, Z. Q. Li, D. N. Basov, M. M. Fogler, Z. Hao and M. C. Martin, *Phys. Rev. B* **78** 235408 (2008).
 - [17] A. B. Kuzmenko, E. van Heumen, D. van der Marel, P. Lerch, P. Blake, K. S. Novoselov, and A. K. Geim, *Phys. Rev. B* **79** 115441 (2009).
 - [18] Y. Zhang, T.-T. Tang, C. Girit, Z. Hao, M. C. Martin, A. Zettl, M. F. Crommie, Y. R. Shen, and F. Wang, *Nature* **459**, 820 (2009).
 - [19] K. F. Mak, C. H. Lui, J. Shan and T. F. Heinz, *arXiv:0905.0923*
 - [20] T. Ohta, A. Bostwick, J. L. McChesney, T. Seyller, K. Horn, and E. Rotenberg, *Phys. Rev. Lett.* **98**, 206802 (2007).
 - [21] J. Guettinger, C. Stampfer, F. Molitor, D. Graf, T. Ihn, and K. Ensslin, *New J. Phys.* **10**, 125029 (2008).
 - [22] M. F. Craciun, S. Russo, M. Yamamoto, J. B. Oostinga, A. F. Morpurgo, and S. Tarucha, *Nat. Nanotechnol.* **4**, 383 (2009).
 - [23] S. Latil and L. Henrard, *Phys. Rev. Lett.* **97**, 036803 (2006).
 - [24] B. Partoens and F. M. Peeters, *Phys. Rev. B* **74**, 075404

- (2006); *ibid.* **75**, 193402 (2007).
- [25] M. Koshino and T. Ando, Phys. Rev. B **76**, 085425 (2007); *ibid.* **77**, 115313 (2008).
- [26] M. Koshino and E. McCann, Phys. Rev. B **79** 125443 (2009).
- [27] A. A. Avetisyan, B. Partoens and F. M. Peeters, Phys. Rev. B **79**, 035421 (2009).
- [28] C.-L. Lu, H.-C. Lin, C.-C. Hwang, J. Wang, M.-F. Lin, and C.-P. Chang, Appl. Phys. Lett. **89**, 221910 (2006).
- [29] J. L. Manes, F. Guinea, and M. A. Vozmediano, Phys. Rev. B **75**, 155424 (2007).
- [30] H. Min and A. H. MacDonald, Phys. Rev. B **77**, 155416 (2008).
- [31] T. Ando, T. Nakanishi, and R. Saito, J. Phys. Soc. Jpn. **67**, 2857 (1998).
- [32] Corners of the hexagonal Brillouin zone are located at wave vector $\mathbf{K}_\xi = \xi(\frac{4}{3}\pi a^{-1}, 0)$, where $\xi = \pm 1$ and a is the lattice constant.
- [33] L. M. Lifshitz, Zh. Exp. Teor. Fiz., **38**, 1565 (1960) [Sov. Phys. JETP **11**, 1130 (1960)]; A. A. Abrikosov, Fundamentals of the Theory of Metals. Elsevier, 1988.
- [34] M. Koshino and T. Ando, Phys. Rev. B **73**, 245403 (2006).
- [35] J. Cserti, A. Csordás and G. Dávid, Phys. Rev. Lett. **99**, 066802 (2007).
- [36] E. McCann, D. S. L. Abergel and V. I. Fal'ko, Solid State Commun. **143**, 110 (2007).
- [37] G. P. Mikitik and Y. Sharlai, Phys. Rev. B **77**, 113407 (2008).
- [38] C. Toke and V. I. Fal'ko, arXiv:0903.2435
- [39] M. S. Dresselhaus and G. Dresselhaus, Adv. Phys. **51**, 1 (2002).
- [40] J. W. McClure, Carbon **7**, 425 (1969).
- [41] D. P. Arovas and F. Guinea, Phys. Rev. B **78**, 245416 (2008).